SUBMITTED TO MAGNETIC RESONANCE IN MEDICINE

Asymptotic Behavior of the Direction-Averaged Diffusion-Weighted MRI Signal using Different B-Tensor Encoding Schemes

Maryam Afzali PhD[1] | Santiago Aja-Fernández PhD[1,2] | Derek K Jones PhD[1,3]

[1]Cardiff University Brain Research Imaging Centre (CUBRIC), School of Psychology, Cardiff University, Cardiff, United Kingdom

[2]Laboratorio de Procesado de Imagen, ETSI Telecomunicación Edificio de las Nuevas Tecnologías, Campus Miguel Delibes s/n, Universidad de Valladolid, 47011 Valladolid, Spain

[3]Mary MacKillop Institute for Health Research, Faculty of Health Sciences, Australian Catholic University, Melbourne, Victoria, 3065, Australia

Correspondence
Maryam Afzali PhD, Cardiff University Brain Research Imaging Centre (CUBRIC), School of Psychology, Cardiff University, Cardiff, United Kingdom
Email: maryam.afzali.m@gmail.com

Present address
[†]Cardiff University Brain Research Imaging Centre (CUBRIC), School of Psychology, Cardiff University, Cardiff, United Kingdom

Funding information
EPSRC Grant: EP/M029778/1 Wellcome Trust Grant: 096646/Z/11/Z and 104943/Z/14/Z. The Ministerio de Ciencia e Innovación of Spain for research grants RTI2018-094569-B-I00 and PRX18/00253.

Purpose: It has been shown previously that for a very specific form of diffusion-encoding, i.e., the conventional Stejskal-Tanner pulsed gradient, or 'linear tensor encoding' (LTE), and in tissue in which diffusion exhibits a 'stick-like' geometry, the diffusion-weighted MRI signal at extremely high b-values follows a power law. Specifically, the signal decays as a $1/\sqrt{b}$. Here, the asymptotic behaviour of the direction-averaged signal for arbitrary diffusion encoding waveforms is considered to establish whether power-law behaviours occur with other encoding wave-forms and for other (non stick-like) diffusion geometries.
Methods: We consider the asymptotic form of the signal decay for high b-values for encoding geometries ranging from 2-dimensional planar tensor encoding (PTE), through isotropic or spherical tensor encoding (STE) to linear tensor encoding. When a power-law behaviour was suggested, this was tested using *in silico* simulations and *in vivo* using an ultra-strong gradient (300 mT/m) Connectom scanner.
Results: Our theoretical derivation shows that a power law only exists for two scenarios: For stick-like geometries, (i) the already-discovered LTE case; and (ii) for pure planar encoding. In this latter case, to first order, the signal decays as $1/b$. Our *in silico* and *in vivo* experiments confirm this $1/b$

relationship.
Conclusion: A complete analysis of the power-law dependencies of the diffusion-weighted signal at high b-values has been performed. Only two forms of encoding result in a power-law dependency, pure linear and pure planar tensor encoding and when the diffusion geometry is 'stick-like'. The different exponents of these encodings could be used to provide independent validation of the presence of stick-like geometries *in vivo*.

KEYWORDS
Diffusion weighted imaging, Direction-averaged diffusion signal, High b-value, B-tensor encoding, Power-law

1 | INTRODUCTION

Pathological disorders happen at the cellular level, therefore, it is important to obtain information on the micrometer scale. Diffusion MRI provides a tool to study brain microstructure based on the Brownian motion of water molecules [1] and it is therefore sensitive to the changes in the microstructure of the tissue [2, 3, 4]. Different mathematical representations are proposed to describe this relationship between the diffusion signal and the changes in the microstructure [5, 6, 7] the most prominent are the bi-exponential [8, 9, 10, 11, 12], the stretched exponential [13] and the power law [14, 15, 16, 17] models. The mathematical forms of these approaches are quite different. In the bi-exponential approach, the large b-value behavior is assumed to be dominated by the intra-axonal compartment. For stretched exponentials, the signal relationship with the b-value is $\exp[-(k\,b)^a]$, where k is a constant and $a < 1$ is the stretching parameter. In the statistical model developed by Yablonskiy et al. [14], the signal decays as $1/b$ for large b, while the other studies [15, 16, 17], have reported that the signal at high b-value, decays as $1/\sqrt{b}$.
The aforementioned studies all used single diffusion encoding (SDE). Since the development of the Pulsed Gradient Spin Echo (PGSE) sequence [18], there have been many works aimed at maximizing the information that can be obtained from a dMRI experiment by exploring different acquisition protocols [19, 20]. One such modification is the addition of multiple gradient pairs. We can use two pairs of pulsed-field gradients (PFGs) to obtain a Double Diffusion Encoding (DDE) [21, 22]. It has been shown that DDE, as well as other multiple encoding schemes such as triple diffusion encoding (TDE) [23], provide information that is not accessible with SDE [24].
This approach has been utilized by several groups for extracting microstructural information [25, 26, 27, 28]. A framework was recently proposed [29] to probe tissue using different q-space trajectory encodings which can be described by a second-order b-tensor. SDE, DDE, and TDE can be characterized by b-tensors, with one, two and three non-zero eigenvalues, respectively. In this framework, SDE is also called Linear tensor encoding (LTE), DDE with perpendicular directions is called planar tensor encoding (PTE) and TDE with equal eigenvalues is called spherical tensor encoding (STE).
In this study, we investigate the effect of different b-tensor encodings on the diffusion signal at high b-values. To remove the effect of fiber orientation distribution [30], the acquired signal is averaged over all diffusion directions for each shell. This so-called powder-averaged signal [31, 32] has less complexity than the direction-dependent signal.

Powder averaging yields a signal whose orientation-invariant aspects of diffusion are preserved but with an orientation distribution that mimics complete dispersion of anisotropic structures.

2 | THEORY

In multi-dimensional diffusion MRI, the b-matrix is defined as $B = b/3(1 - b_\Delta)I_3 + bb_\Delta \mathbf{g}\mathbf{g}^T$, where $\mathbf{g}$ is the diffusion gradient direction and the b-value, b, is defined as the trace of the b-matrix. The eigenvalues of the b-matrix are $b_{||}$, $b_\perp^{(1)}$ and $b_\perp^{(2)}$ where $b_\perp^{(1)} = b_\perp^{(2)} = b_\perp$ and $b_{||}$ is the largest. b_Δ is defined as $b_\Delta = \frac{b_{||} - b_\perp}{b_{||} + 2b_\perp}$. Changing b_Δ, we can generate different types of b-tensor encoding. For LTE, PTE, and STE, $b_\Delta = 1, -1/2$, and 0 respectively [23].
For the powder-averaged signal, the diffusion attenuation is a function of the orientation-invariant aspects of the diffusion and the encoding. The compartment diffusion attenuation is (Eq. (2) in [33]):

$$S(b) = \frac{\sqrt{\pi} e^{-\frac{b}{3}(D^{||} + 2D^\perp - b_\Delta(D^{||} - D^\perp))} \operatorname{erf}(\sqrt{bb_\Delta(D^{||} - D^\perp)})}{2\sqrt{bb_\Delta(D^{||} - D^\perp)}} \tag{1}$$

where S is the normalized diffusion signal and $D^{||}$ and $D^\perp$ are the the parallel and perpendicular diffusivities respectively. We use the subscript "$_e$" and "$_a$" to denote the parameters of the extra- and intra-axonal compartments respectively. Here, we study the effect of b-tensor shape on the diffusion-weighted signal at high b-values. We begin with linear, planar and spherical before considering general b-tensor shapes.

2.1 | Different B-Tensor Encoding Schemes

2.1.1 | LTE

In linear tensor encoding, $b_\Delta = 1$ and assuming stick-like geometry, $D^\perp = 0$ in Eq. (1), therefore S_{ic} has the following form:

$$S_{ic}^{LTE}(b) = \frac{\sqrt{\pi} \operatorname{erf}(\sqrt{bD_a{}^{||}})}{2\sqrt{bD_a{}^{||}}} \tag{2}$$

Because $bD_a{}^{||} \gg 1$ for large b-values (b > 7000 s/mm^2), $\operatorname{erf}(\sqrt{bD_a{}^{||}}) = 1$ and the power-law scaling [17] for the intra-axonal compartment becomes:

$$S_{ic}^{LTE}(b) = \frac{\sqrt{\pi}}{2\sqrt{bD_a{}^{||}}} \tag{3}$$

The sensitivity of MR to axon radius would alter the $b^{-1/2}$ scaling [34] because there will be a perpendicular diffusivity and the exponential term in Eq. (1) will not be zero. For large b-values, the extra-axonal signal (see Appendix A) decays exponentially faster than the intra-axonal compartment ($\exp(-bD_e{}^\perp) \ll 1$) and therefore, can be neglected.

2.1.2 | PTE

In planar tensor encoding, $b_\Delta = -1/2$ and S_{ic} has the following form:

$$S_{ic}^{PTE}(b) = \frac{\sqrt{\pi} e^{\frac{-bD_a{}^{||}}{2}} \operatorname{erfi}(\sqrt{bD_a{}^{||}/2})}{2\sqrt{bD_a{}^{||}/2}} \tag{4}$$

For large b-values, $bD_a{}^{||} \gg 1$, therefore the diffusion signal can be approximated by the following equation (see Appendix A):

$$S_{ic}^{PTE}(b) = \frac{1}{bD_a{}^{||}} \sum_{k=0}^{N} \frac{(2k-1)!!}{(bD_a{}^{||})^k} \tag{5}$$

where !! denotes the double factorial and N depends on the $bD_a{}^{||}$ value (Fig. 1 and Table 1).
For large b-values, the extra-axonal signal decays exponentially faster than the intra-axonal compartment, $\exp(-bD_e{}^{\perp}) \ll 1$, (see Appendix A) and can be neglected.

2.1.3 | STE

In spherical tensor encoding, $b_\Delta = 0$ and S_{ic} has the following form:

$$S_{ic}^{STE}(b) = e^{-\frac{b}{3}D_a{}^{||}} \tag{6}$$

For large b-values, both intra- and extra-axonal signals decay exponentially fast, $\exp(-\frac{bD_a{}^{||}}{3}) \ll 1$, $\exp(-\frac{b(D_e{}^{||}+2D_e{}^{\perp})}{3}) \ll 1$ and both of them are negligible (see Appendix A). Therefore, the spherical tensor encoding does not provide a considerable signal for large b-values in a two-compartment model.

2.2 | General Case

Here, we consider the general case of $b_\Delta \neq 0$, to cover all b-tensor shapes between $b_\Delta = -0.5$ (PTE) to $b_\Delta = 1$ (LTE).

2.2.1 | $0 < b_\Delta \leq 1$

As noted above, in this range the error function in Eq. (1) goes to 1 for high b. To have a power-law relationship between the signal and the b-value, the exponential term $\exp[-b(D^{||} + 2D^{\perp} - b_\Delta(D^{||} - D^{\perp}))/3]$ should go to one and therefore $D^{||} + 2D^{\perp} - b_\Delta(D^{||} - D^{\perp}) = 0$. Then we have:

$$\frac{D^{\perp}}{D^{||}} = \frac{b_{\Delta} - 1}{b_{\Delta} + 2} \tag{7}$$

which is only physically plausible (i.e. the ratio of diffusion coefficients has to be ≥ 0) for $b_{\Delta} - 1 \geq 0$, but the maximum value that b_{Δ} can take is one, and therefore $D^{\perp}$ has to be zero to satisfy Eq. (7) i.e. the geometry has to be that of a stick, and the b-tensor has to be a pure LTE to have a power-law relationship.

2.2.2 | $-0.5 \leq b_{\Delta} < 0$

Conversely, in the range $-0.5 \leq b_{\Delta} < 0$, as in Eq. (4), the error function becomes imaginary. Similar to the first scenario, to have a power-law relationship the exponential term has to be one. By replacing the first term of the approximation in Eq. (16) into Eq. (1), we have:

$$S(k = 0) = \frac{e^{\frac{-b}{3}[(D^{||}+2D^{\perp})-b_{\Delta}(D^{||}-D^{\perp})]-bb_{\Delta}(D^{||}-D^{\perp})}}{-2bb_{\Delta}(D^{||} - D^{\perp})} \tag{8}$$

To have the exponential equal to one:

$$\frac{D^{\perp}}{D^{||}} = \frac{2b_{\Delta} + 1}{2b_{\Delta} - 2} \tag{9}$$

where the right side of the equation is negative for $-0.5 < b_{\Delta} < 0$ which is not physically plausible for the left side of the equation (i.e. ratio of diffusivities). Therefore, the only possible case is to have $D^{\perp} = 0$ which again means stick-like geometry and $b_{\Delta} = -0.5$ which is pure PTE. Clearly the exponential term will become zero if and only if $b_{\Delta} = -0.5$, and thus the $1/b$ signal form will occur if and only if the b-tensor shape has just 2 non-zero eigenvalues, i.e. pure PTE. Thus, for stick-like geometries, there are only two b-tensor shapes for which a power-law exists: pure linear and pure planar. As the above equations show, we do not observe a power-law for non-stick-like geometries.

2.3 | Simulations

Synthetic data were generated with 30 diffusion encoding gradient orientations uniformly distributed on the unit sphere [35, 36] and 21 b-values spaced in the interval [0, 10000 s/mm^2] with a step-size of 500 s/mm^2. The noise is considered Rician with SNR = 250 for the b0 image, which is practically feasible using the Connectom scanner [37] with an echo time of $88ms$ [38]. A two-compartment model with a Watson orientation distribution function is used:

$$S/S_0 = f \int_{\mathbb{S}^2} W(\mathbf{n}) S_{cyl}(\mathbf{n}) d\mathbf{n} + (1 - f) \int_{\mathbb{S}^2} W(\mathbf{n}) S_{ec}(\mathbf{n}) d\mathbf{n} \tag{10}$$

where $W(\mathbf{n})$ is the Watson ODF and S_{cyl} is the signal attenuation of the impermeable cylinders [39] in the presence of b-tensor encoding [40] (Appendix B). The ground truth parameter values defined by a set of parameters [f = 0.65, $D_a{}^{||}$ = 2 $\mu m^2/ms$, $D_e^{||}$ = 2 $\mu m^2/ms$, $D_e^{\perp}$ = 0.25, 0.5, 0.75 $\mu m^2/ms$ and κ = 11] and axon radius r_i, come from the bins of the histograms in [41]. We average the signal over all r_is weighted by r_i^2. In histology, there is a possibility of tissue shrinkage. To account for this change, the axon radius values are multiplied with three shrinkage factors $\eta = 0, 1, 1.5$ [41, 42]. The $\eta = 0$ case simulates the effect of zero-radius axons. The noisy diffusion signal is modeled according to the following:

$$S_n = \sqrt{(S + N_r(0,\sigma))^2 + N_i(0,\sigma)^2} \tag{11}$$

where S_n and S are the noisy and noise-free signal respectively and N_r and N_i are the normal distributed noise in the real and imaginary images respectively with a standard deviation of σ [43, 44].

2.4 | *In vivo* Data

Two healthy participants who showed no evidence of a clinical neurologic condition were scanned in this study that was conducted with approval of the Cardiff University School of Medicine ethics committee. Diffusion-weighted images were acquired with 30 gradient directions for planar tensor encoding (PTE) on a 3T Connectom MR imaging system (Siemens Healthineers, Erlangen, Germany). Twenty axial slices with a voxel size of $4mm$ isotropic (given the strong signal attenuations investigated here, a low resolution of 4 mm isotropic was used) and a 64×64 matrix size, TE = 88 ms, TR = 4300 ms, were obtained for each individual.
Diffusion data were acquired for 10 b-value shells from 1000 to 10000 s/mm^2 with a step size of 1000 and each shell had the same 30 diffusion encoding gradient orientations uniformly distributed on the unit sphere. One b0 image was acquired between each b-value shell as a reference.
The data were corrected for Gibbs ringing [45], eddy current distortions and subject motion [46]. We normalized the direction-averaged signal based on the b0 signal in each voxel.

3 | RESULTS

The asymptotic expansion of erfi(x) in Eq. 16 (see Appendix A) is valid when $x \to \infty$, but large values of $bD_a{}^{||}$ would suppress the signal to immeasurable levels, and therefore there are practical bounds on the value of $bD_a{}^{||}$ that can be achieved. Therefore, we compared the original signal in Eq. 4 and the approximated signal using Eq. 5 for different values of N and $bD_a{}^{||}$ (Fig. 1 and Table 1). We use a normalized error to compare the original (Eq. 4) and the approximated signal (Eq. 5):

$$Normalized\ error = \frac{|S - \hat{S}|}{S} = |1 - \frac{\hat{S}}{S}| \tag{12}$$

where S is the original signal obtained from Eq. 4 and $\hat{S}$ is the approximated signal from Eq. 5.
Fig. 1 shows $\hat{S}/S$ for $3 < bD_a{}^{||} < 20$ and $4 < N < 21$. The selected range of $bD_a{}^{||}$ is compatible with the range of

b-values that we can obtain from the Connectom scanner and also the range of $D_a^{||}$ that exist in the brain [47]. Based on Fig. 1 the number of terms in Eq. 10 should be smaller than or equal to the $bD_a^{||}$ ($N \leq \lfloor bD_a^{||} \rfloor$ where $\lfloor \ldots \rfloor$ denotes the floor function) to have the minimum error ($\hat{S}/S$ is close to one). As the number of terms goes beyond the $bD_a^{||}$, the error increases. Table 1 shows the minimum number of terms, N, for different error threshold values (0.01-0.06). When the error threshold is 0.02, we can approximate Eq. 4 with the first term in Eq. 5 if $bD_a^{||} \geq 14$. For the error threshold of 0.06, the maximum $bD_a^{||}$ to approximate the signal with the first term is 3.

Diffusion MRI is an inherently low SNR measurement technique, particularly when strong diffusion weightings are

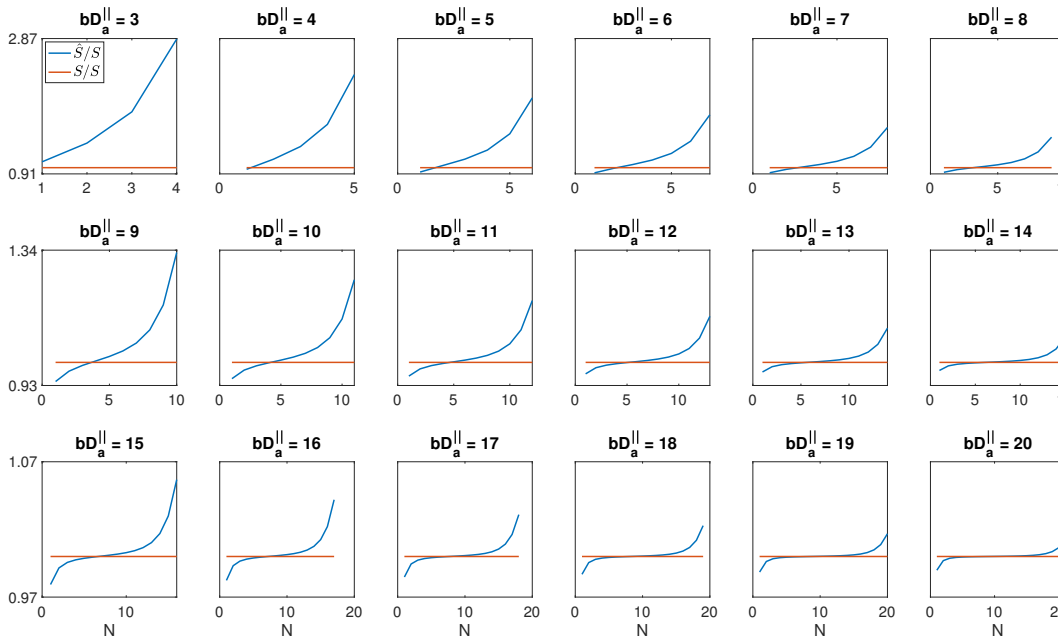

FIGURE 1 The approximated signal over the original PTE signal ($\hat{S}/S$), for different N values.

TABLE 1 The minimum number of terms for reconstructing the PTE signal for different error threshold values.

		$bD_a^{||}$																	
		3	4	5	6	7	8	9	10	11	12	13	14	15	16	17	18	19	20
Error threshold	0.06	1	1	1	1	1	1	1	1	1	1	1	1	1	1	1	1	1	1
	0.05	-	1	1	2	2	1	1	1	1	1	1	1	1	1	1	1	1	1
	0.04	-	1	2	2	2	2	2	1	1	1	1	1	1	1	1	1	1	1
	0.03	-	1	2	2	2	2	2	2	1	1	1	1	1	1	1	1	1	1
	0.02	-	1	-	2	2	2	2	2	2	2	2	1	1	1	1	1	1	1
	0.01	-	-	-	2	3	3	3	3	3	3	2	2	2	2	2	1	1	1

utilized. To reach the level that enables us to approximate the planar diffusion signal in Eq. 4 with the first term of Eq. 5, we need to use relatively high b-values ($bD_a^{||} \geq 14$). One of the challenges with the high b-values is the noise, as the signal amplitude can be close to the noise floor. Therefore, here we find the maximum value of $bD_a^{||}$ that we can use

before hitting this rectified noise floor (see Appendix C).

The noise in complex MR data is normally distributed, whereas the noise in magnitude images is Rician distributed [43, 44]. Here, we select a minimum SNR value equal to 2 (see Appendix C). By setting the diffusion-weighted intensity in Eqs. (2), (4), and (6) to the mean background signal, we obtain the b-value that makes the signal equal to the noise floor.

Fig. 2 shows the maximum $bD_a^{||}$ as a function of SNR for different encoding schemes and different noise floors. The maximum value of $bD_a^{||}$ that can be used while staying above the noise floor increases when SNR increases, but the rate of this change is different for different encoding schemes. The maximum $bD_a^{||}$ value ($bD_a^{||^{max}}$) is proportional to the square of SNR, ($bD_a^{||^{max}} \sim SNR^2$) for LTE, where this relationship is linear for PTE ($bD_a^{||} \sim SNR$) and it is logarithmic for STE ($bD_a^{||} \sim \ln(SNR)$). Based on this plot, if SNR = 50 the values of $bD_a^{||^{max}}$ for linear, planar and spherical tensor encoding schemes are around 312, 21 and 9 respectively. The SNR in our data is around 250 [38] therefore the measured signal values in our experiment are higher than the noise level. For this SNR, the $bD_a^{||^{max}}$ for linear, planar and spherical tensor encoding schemes are around 15625, 100 and 16 respectively.

Fig. 3 shows the simulated direction-averaged PTE signal as a function of $1/b$ for three different perpendicular

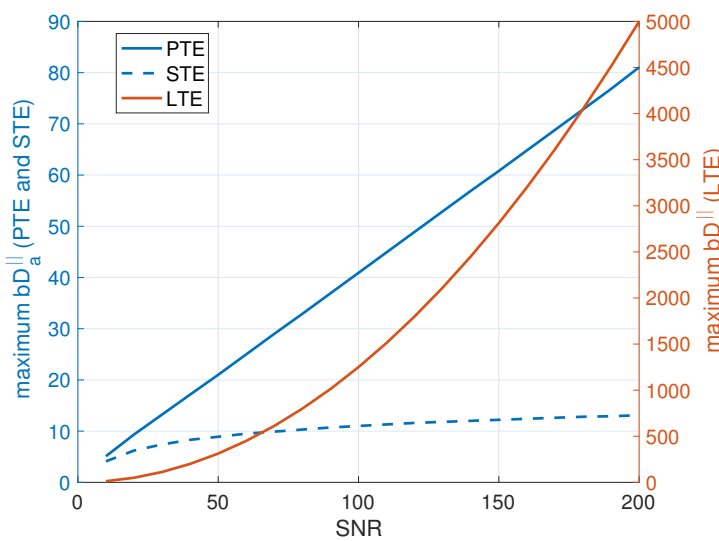

FIGURE 2 Maximum $bD_a^{||}$ vs SNR. The Maximum $bD_a^{||}$ value is proportional to the square of SNR, ($bD_a^{||} \sim SNR^2$) for LTE, where this relationship is linear for PTE ($bD_a^{||} \sim SNR$) and it is logarithmic for STE ($bD_a^{||} \sim \ln(SNR)$).

diffusivities and three different shrinkage factors. The result of the power-law fit ($S = \beta b^{-\alpha}$) is represented by the red dashed line and the α and β values are reported in each plot. In our simulation, f = 0.65, $D_a^{||}$ = 2 $\mu m^2/ms$, therefore if the approximation in Eq. 5 is valid, $\beta \approx 0.325$ and $\alpha \approx 1$ indicate that the fit approximately matches the theory.

Fig. 4 illustrates the direction-averaged diffusion signal of the *in vivo* data for different b-values. For high b-values ($7000 < b < 10000 s/mm^2$) the amount of the signal is considerable compared to the noise and the white matter structure is completely clear in the images because of high SNR. The posterior part of the cortex appears bright in the lower b-value images. This may be due to proximity to the coil. These regions were excluded from the analysis.

Fig. 5 shows the parametric map of the exponent α, the histogram of α values for white matter, gray matter, CSF and the

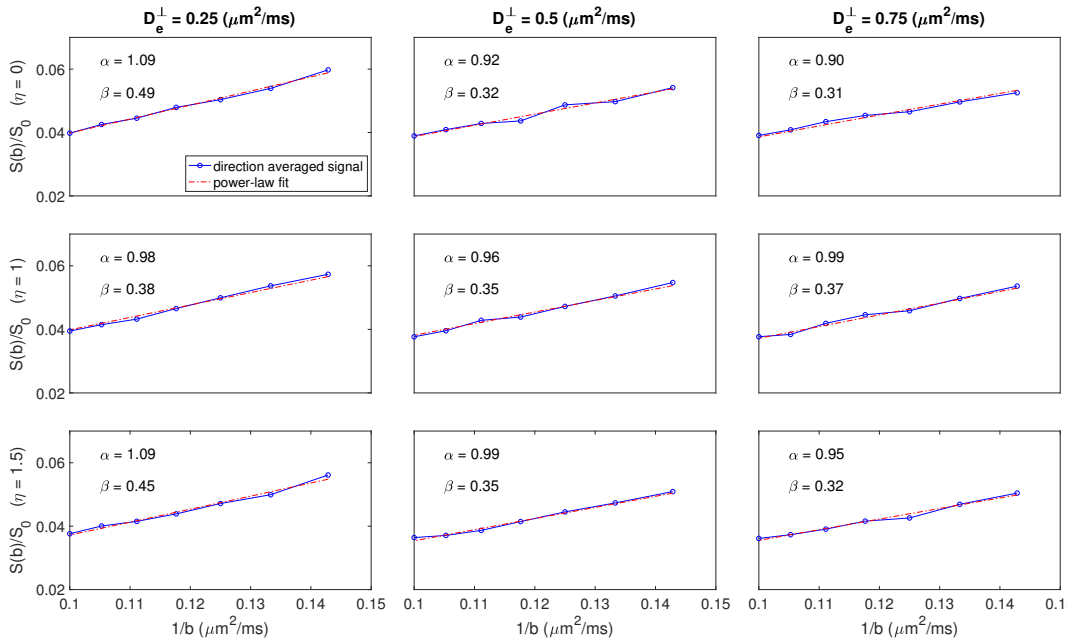

FIGURE 3 Simulated direction-averaged PTE signal for $7000 < b < 10000 s/mm^2$ and the results of the power-law fit.

FA map. To segment the brain image into different tissues, we used FAST (FMRIB's Automated Segmentation Tool) in FSL [48]. In the WM, the α value is close to one, supporting the theory. In grey matter and CSF, the exponent is larger (1.16 and 1.26, respectively). According to the theory outlined above, this would be consistent with a lack of pure 'stick-like' geometry in these tissue components. The spatial resolution of the data must be recognized, i.e., at 4 mm isotropic voxels, obtaining a 'pure' GM signal and 'pure' CSF signal is challenging. It is likely that the intermediate exponent in the GM between that of the WM and CSF is partly attributable to a partial volume effect, and partly attributable to the inadequacy of the model for grey matter architecture. Further investigation of this phenomenon in grey matter is beyond the scope of this work.

Fig. 6 shows the PTE signal of the white matter voxels, the mean value, standard deviation of the signal and the result of the power-law fit over the range of b-values investigated. The results show that the data are well described by power-law behavior, with $\alpha \approx 1$ which confirms the validity of the signal approximation using the first term in Eq. 5.

4 | DISCUSSION

The main finding of this paper is a theoretical derivation, and confirmation *in silico* and *in vivo* of a power-law relationship between the direction-averaged DWI signal and the b-value using planar tensor encoding, as given by Eq. 5, for b-values ranging from 7000 to 10000 s/mm^2. In white matter, the average value of the estimated exponent is $\alpha = 1.02 \pm 0.02$. For smaller b-values, this behavior must break down as the DWI signal of PTE cannot be approximated by Eq. 5 (Fig. 1) and also we cannot neglect the contribution of the extracellular compartment. It could also fail for very large b-values, if

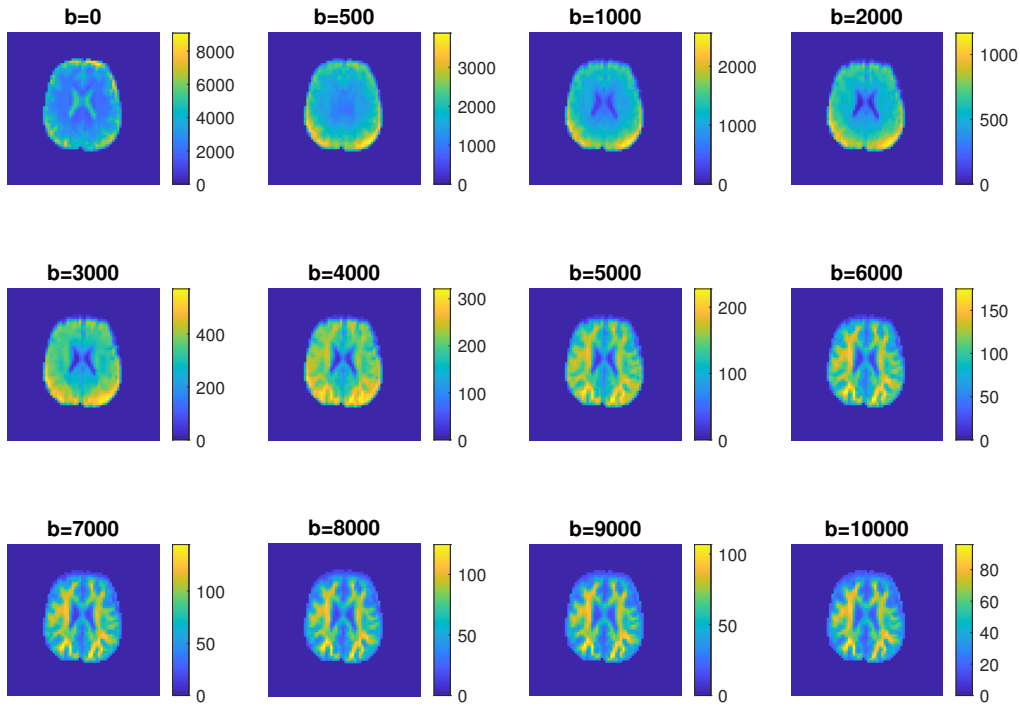

FIGURE 4 Direction-averaged diffusion signal for different b-values (b = 0 to 10000 s/mm^2) in PTE.

there were immobile protons that contributed a constant offset to the overall signal or if there is any sensitivity to the axon diameter [34].

The exponent of approximately one for white matter using PTE is consistent with the large b-value limit predicted for a model of water confined to sticks Eq. 5, which is used to describe the diffusion dynamics of intra-axonal water. Our results confirm this relationship between the diffusion signal and the b-value (Fig. 6).

The $b^{-1/2}$-scaling has previously been suggested by [17, 16] for linear tensor encoding. Two other proposed models predict power law signal decay, for large b-values using a linear tensor encoding. One of these is the statistical model [14], where the signal decays as 1/b for large b. Some other models [49, 50, 51], assume a gamma distribution for the diffusion coefficients and the signal has the following form:

$$\frac{S}{S_0} = \frac{1}{(1 + b/b_c)^{\epsilon}} \tag{13}$$

which scales as $(b_c/b)^{\epsilon}$ for $b \gg b_c$. However, in this case, the exponent ϵ does not have a universal value, it depends on the distribution.

This work interprets the diffusion-weighted MRI signal decay at high b-values in the form of $S \sim b^{-1}$ for planar tensor encoding. An important application of this finding is using the combination of linear and planar tensor encodings to

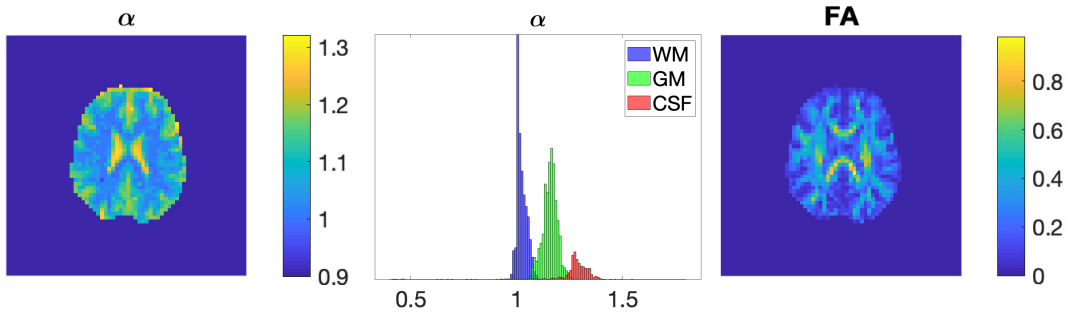

FIGURE 5 Parametric map of the exponent α, the histogram of α values and FA using planar tensor encoding

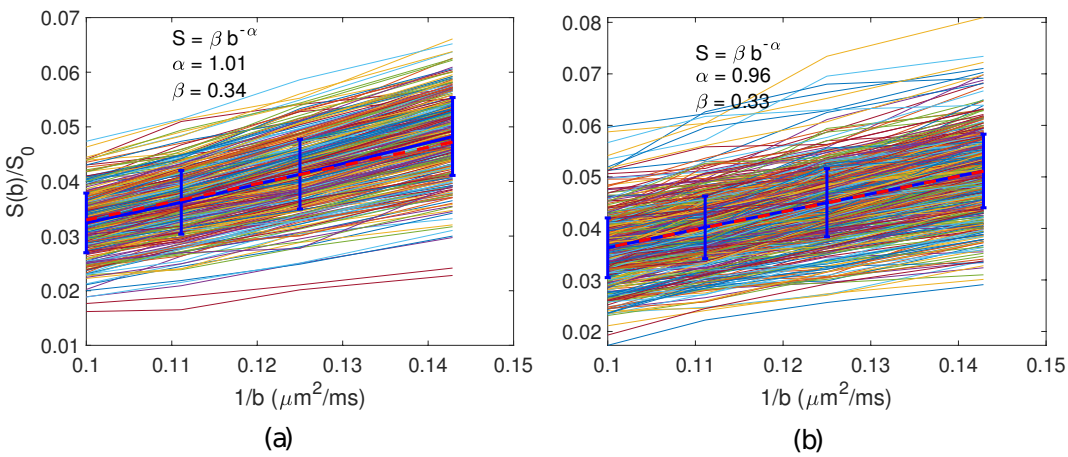

FIGURE 6 The plot of the diffusion signal vs $1/b$ for *in vivo* white matter voxels of (a) first participant, (b) second participant, using planar tensor encoding. The blue curve with the error bar shows the mean and the std of the average signal and the red line shows the power-law fit. The parameters, α and β are reported in the figure. $\alpha = 1$ shows the power-law relationship between the diffusion signal and the b-value.

characterize the intra-axonal diffusivity and the signal fraction as it is proposed by [52] using triple diffusion encoding.

5 | CONCLUSION

This work explores the diffusion-weighted MRI signal decay at high b-values for planar, and spherical tensor encoding complementing and extending previous works on linear tensor encoding. By exploring diffusion averaged signals, we conclude that the signal from STE decays exponentially for all the range of b-values. The intra-axonal signal does not decay exponentially as a function of b for linear and planar tensor encoding in high b-values. The direction-averaged DWI signal of PTE and LTE decreases with increasing b-values as a power law, for b-values ranging from 7000 to 10000 s/mm^2. In white matter, the exponent characterizing this decrease is close to one-half, for LTE and one for PTE, which is consistent with the large b-value limit of a model in which intra-axonal water diffusion is confined to sticks. Obtaining an exponent of -1 for PTE and -1/2 for LTE could provide useful cross-validation of the presence of stick-like geometries

in tissue. A complete analysis of the power-law dependencies of the diffusion-weighted signal at high b-values has been performed. Only two forms of encoding result in a power-law dependency, pure linear and pure planar tensor encoding. The different exponents of these encodings could be used to provide independent validation of the presence of stick-like geometries *in vivo* where, due to the slower decay, LTE is the most SNR efficient method. Any deviation from the power-law could indicate deviation from stick-like geometry with both LTE and PTE encoding, as exploited by [34] for estimating the effective radius of axons. Again, for such applications of the power-law, the LTE approach is to be favoured over the PTE approach, on account of the higher SNR per unit time.

A | DIFFERENT B-TENSOR ENCODING SCHEMES

A.1 | LTE

In linear tensor encoding, $b_\Delta = 1$ and S_{ec} has the following form:

$$S_{ec}^{LTE}(b) = \frac{\sqrt{\pi} e^{-bD_e{}^{\perp}} \operatorname{erf}(\sqrt{b(D_e{}^{||} - D_e{}^{\perp})})}{2\sqrt{b(D_e{}^{||} - D_e{}^{\perp})}} \tag{14}$$

A.2 | PTE

In planar tensor encoding, $b_\Delta = -1/2$ and S_{ic} has the following form:

$$S_{ic}^{PTE}(b) = \frac{\sqrt{\pi} e^{\frac{-bD_a{}^{||}}{2}} \operatorname{erfi}(\sqrt{bD_a{}^{||}/2})}{2\sqrt{bD_a{}^{||}/2}} \tag{15}$$

Asymptotic expansion of $\operatorname{erfi}(x)$ is as follows:

$$\operatorname{erfi}(x) = \frac{e^{x^2}}{x\sqrt{\pi}} \sum_{k=0}^{\infty} \frac{(2k-1)!!}{(2x^2)^k} \tag{16}$$

where $x \to \infty$ and $(-1)!! = 1$.
$bD_a{}^{||} \gg 1$ for large b, therefore we have:

$$S_{ic}^{PTE}(b) = \frac{1}{bD_a{}^{||}} \sum_{k=0}^{N} \frac{(2k-1)!!}{(bD_a{}^{||})^k} \tag{17}$$

where N depends on the $bD_a{}^{||}$ value (Fig. 1 and table 1).

$$S_{ic}^{PTE}(b) = \frac{1}{bD_a{}^{||}}(1 + \frac{1}{bD_a{}^{||}} + \frac{3}{(bD_a{}^{||})^2} + \ldots) \tag{18}$$

The extra-axonal signal decays exponentially faster than the intra-axonal compartment for large b, $e^{-bD_e{}^{\perp}} \ll 1$, and can be neglected.

$$S_{ec}^{PTE}(b) = \frac{\sqrt{\pi}e^{-\frac{b}{2}(D_e{}^{||}+D_e{}^{\perp})}\,\mathrm{erfi}(\sqrt{b(D_e{}^{||}-D_e{}^{\perp})/2})}{2\sqrt{b(D_e{}^{||}-D_e{}^{\perp})/2}} \tag{19}$$

A.3 | STE

In spherical tensor encoding, $b_\Delta = 0$ and S_{ec} has the following form:

$$S_{ec}^{STE}(b) = e^{-\frac{b}{3}(D_e{}^{||}+2D_e{}^{\perp})} \tag{20}$$

B | SIGNAL ATTENUATION IN A CYLINDRICAL PORE USING PTE

The signal attenuation of the impermeable cylinders [39] using PTE is generated using the following equation [40]:

$$S_{cyl} = S_{cyl}{}^{||}S_{cyl}^{\perp} \tag{21}$$

$$S_{cyl}{}^{||} = e^{-\frac{b}{2}D_a{}^{||}(1-(\mathbf{g}.\mathbf{n})^2)} \tag{22}$$

$$\ln(S_{cyl}^{\perp}) = -\frac{2\gamma^2G^2(1+(\mathbf{g}.\mathbf{n})^2)R^6}{(D_a{}^{||})^2}\sum_{n=1}^{\infty}\frac{A_n}{\alpha_n^6(\alpha_n^2-1)} \tag{23}$$

where α_n is the root of the derivatives of the first order Bessel function $J_1'(\alpha_n) = 0$ and

$$A_n = \frac{2\alpha_n^2D_a{}^{||}\delta}{R^2} - 2 + 2L_n(\delta) - L_n(\Delta-\delta) + 2L_n(\Delta) - L_n(\Delta+\delta) \tag{24}$$

and

$$L_n(t) = e^{-\frac{\alpha_n^2 D_a||_t}{R^2}} \tag{25}$$

C | SNR AND ERROR

Let us assume that a real signal S follows a Rician distribution with parameters A and σ

$$S \sim R(A, \sigma) \tag{26}$$

with PDF [43]

$$p(x|A, \sigma) = \frac{x}{\sigma^2} e^{-\frac{x^2+A^2}{2\sigma^2}} I_0\left(\frac{Ax}{\sigma^2}\right) u(x), \tag{27}$$

where A is the (absolute value) of the original signal (without noise) and σ^2 is the variance of the complex Gaussian noise. It can be seen as

$$S = \sqrt{(A + N_r(0, \sigma))^2 + N_i(0, \sigma))^2}. \tag{28}$$

The question in MRI of how low can we go with the signal (i.e., when do we reach the noise floor) will always depend on the application and on the estimator we are using. However, we can always consider a lower bound to the SNR related to the error of the measured signal.
To calculate an SNR *threshold* independent of the particular application, we can use two different definitions of error: (1) the Mean Square Error (MSE) or (2) the mean error (ME). We define the MSE as

$$\text{MSE} = E\left\{(S - A)^2\right\} \tag{29}$$

where S is the measured signal and A is the *original* signal. We use the mean value to assure that this error is a statistical property and not an isolated measure. The ME is alternatively define as:

$$\text{ME} = E\left\{S - A\right\}. \tag{30}$$

For the SNR calculation, we will consider that the error committed is a percentage of the original signal (to make it signal dependent), i.e.

$$\begin{aligned} E\left\{(S - A)^2\right\} &< \epsilon \cdot A^2 \\ E\left\{\left(\frac{S}{A} - 1\right)^2\right\} &< \epsilon. \end{aligned}$$

Alternatively, for the ME:

$$\begin{aligned} E\left\{S-A\right\} &< \epsilon \cdot A \\ E\left\{\frac{S}{A}-1\right\} &< \epsilon. \end{aligned}$$

Assuming a Rician distribution of parameters A and σ, the errors become:
The MSE:

$$E\left\{\left(\frac{S}{A}-1\right)^2\right\} = 2+\frac{2}{\mathrm{SNR}^2}-\sqrt{2\pi}\frac{1}{\mathrm{SNR}}L_{1/2}\left(-\frac{\mathrm{SNR}^2}{2}\right)$$

The ME:

$$E\left\{\frac{S}{A}-1\right\} = \sqrt{\frac{\pi}{2}}\frac{1}{\mathrm{SNR}}L_{1/2}\left(-\frac{\mathrm{SNR}^2}{2}\right)-1.$$

For the sake of simplicity, in this paper, we will consider ME as an error measure, since MSE is more restrictive. The relation between ME and SNR for different errors can be seen in Table 2.

TABLE 2 SNR values for different errors for the Rician model.

Error	$< 0.005A$	$< 0.05A$	$0.1A$	$0.2A$	$< 0.5A$
ME	SNR$>$ 10	SNR$>$ 3.21	SNR$>$ 2.30	SNR$>$ 1.67	SNR$>$ 1.05

ACKNOWLEDGEMENTS

The data were acquired at the UK National Facility for *In Vivo* MR Imaging of Human Tissue Microstructure funded by the EPSRC (grant EP/M029778/1), and The Wolfson Foundation. This work was supported by a Wellcome Trust Investigator Award (096646/Z/11/Z) and a Wellcome Trust Strategic Award (104943/Z/14/Z). S. Aja-Fernandez acknowledges the Ministerio de Ciencia e Innovación of Spain for research grants RTI2018-094569-B-I00 and PRX18/00253 (Estancias de profesores e investigadores senior en centros extranjeros). We are grateful to Emre Kopanoglu for feedback on the manuscript. We thank Zahra Moradi and Lars Mueller for help with the data acquisition. We thank Chantal Tax for help with the data acquisition and feedback on the manuscript. The authors would like to thank Filip Szczepankiewicz and Markus Nilsson for providing the pulse sequences for b-tensor encoding.

REFERENCES

[1] Tanner J. Self diffusion of water in frog muscle. Biophysical journal 1979;28(1):107.

[2] Callaghan P, Eccles C, Xia Y. NMR microscopy of dynamic displacements: k-space and q-space imaging. Journal of Physics E: Scientific Instruments 1988;21(8):820.

[3] Basser PJ, Mattiello J, LeBihan D. MR diffusion tensor spectroscopy and imaging. Biophysical journal 1994;66(1):259–267.

[4] Jones DK. Diffusion MRI. Oxford University Press; 2010.

[5] Panagiotaki E, Schneider T, Siow B, Hall MG, Lythgoe MF, Alexander DC. Compartment models of the diffusion MR signal in brain white matter: a taxonomy and comparison. Neuroimage 2012;59(3):2241–2254.

[6] Mulkern RV, Haker SJ, Maier SE. On high b diffusion imaging in the human brain: ruminations and experimental insights. Magnetic resonance imaging 2009;27(8):1151–1162.

[7] Novikov DS, Fieremans E, Jespersen SN, Kiselev VG. Quantifying brain microstructure with diffusion MRI: Theory and parameter estimation. arXiv preprint arXiv:161202059 2016;.

[8] Niendorf T, Dijkhuizen RM, Norris DG, van Lookeren Campagne M, Nicolay K. Biexponential diffusion attenuation in various states of brain tissue: implications for diffusion-weighted imaging. Magnetic Resonance in Medicine 1996;36(6):847–857.

[9] Clark CA, Le Bihan D. Water diffusion compartmentation and anisotropy at high b values in the human brain. Magnetic Resonance in Medicine: An Official Journal of the International Society for Magnetic Resonance in Medicine 2000;44(6):852–859.

[10] Clark CA, Hedehus M, Moseley ME. In vivo mapping of the fast and slow diffusion tensors in human brain. Magnetic Resonance in Medicine: An Official Journal of the International Society for Magnetic Resonance in Medicine 2002;47(4):623–628.

[11] Mulkern RV, Gudbjartsson H, Westin CF, Zengingonul HP, Gartner W, Guttmann CR, et al. Multi-component apparent diffusion coefficients in human brain. NMR in Biomedicine: An International Journal Devoted to the Development and Application of Magnetic Resonance In Vivo 1999;12(1):51–62.

[12] Maier SE, Mulkern RV. Biexponential analysis of diffusion-related signal decay in normal human cortical and deep gray matter. Magnetic resonance imaging 2008;26(7):897–904.

[13] Bennett KM, Schmainda KM, Bennett R, Rowe DB, Lu H, Hyde JS. Characterization of continuously distributed cortical water diffusion rates with a stretched-exponential model. Magnetic Resonance in Medicine: An Official Journal of the International Society for Magnetic Resonance in Medicine 2003;50(4):727–734.

[14] Yablonskiy DA, Bretthorst GL, Ackerman JJ. Statistical model for diffusion attenuated MR signal. Magnetic Resonance in Medicine: An Official Journal of the International Society for Magnetic Resonance in Medicine 2003;50(4):664–669.

[15] Jensen JH, Glenn GR, Helpern JA. Fiber ball imaging. Neuroimage 2016;124:824–833.

[16] McKinnon ET, Jensen JH, Glenn GR, Helpern JA. Dependence on b-value of the direction-averaged diffusion-weighted imaging signal in brain. Magnetic resonance imaging 2017;36:121–127.

[17] Veraart J, Fieremans E, Novikov DS. On the scaling behavior of water diffusion in human brain white matter. NeuroImage 2019;185:379–387.

[18] Stejskal EO, Tanner JE. Spin diffusion measurements: spin echoes in the presence of a time-dependent field gradient. The journal of chemical physics 1965;42(1):288–292.

[19] Jones DK. The effect of gradient sampling schemes on measures derived from diffusion tensor MRI: a Monte Carlo study. Magnetic Resonance in Medicine: An Official Journal of the International Society for Magnetic Resonance in Medicine 2004;51(4):807–815.

[20] Alexander DC. A general framework for experiment design in diffusion MRI and its application in measuring direct tissue-microstructure features. Magnetic Resonance in Medicine: An Official Journal of the International Society for Magnetic Resonance in Medicine 2008;60(2):439–448.

[21] Cory D, Garroway A, Miller J. Applications of spin transport as a probe of local geometry. In: Abstracts of Papers of the American Chemical Society, vol. 199 AMER CHEMICAL SOC 1155 16TH ST, NW, WASHINGTON, DC 20036; 1990. p. 105–POLY.

[22] Shemesh N, Jespersen SN, Alexander DC, Cohen Y, Drobnjak I, Dyrby TB, et al. Conventions and nomenclature for double diffusion encoding NMR and MRI. Magnetic resonance in medicine 2016;75(1):82–87.

[23] Topgaard D. Multidimensional diffusion MRI. Journal of Magnetic Resonance 2017;275:98–113.

[24] Mitra PP. Multiple wave-vector extensions of the NMR pulsed-field-gradient spin-echo diffusion measurement. Physical Review B 1995;51(21):15074.

[25] Özarslan E, Shemesh N, Basser PJ. A general framework to quantify the effect of restricted diffusion on the NMR signal with applications to double pulsed field gradient NMR experiments. The Journal of chemical physics 2009;130(10):104702.

[26] Jespersen SN, Lundell H, Sønderby CK, Dyrby TB. Orientationally invariant metrics of apparent compartment eccentricity from double pulsed field gradient diffusion experiments. NMR in Biomedicine 2013;26(12):1647–1662.

[27] Benjamini D, Komlosh ME, Basser PJ, Nevo U. Nonparametric pore size distribution using d-PFG: comparison to s-PFG and migration to MRI. Journal of Magnetic Resonance 2014;246:36–45.

[28] Ianuş A, Drobnjak I, Alexander DC. Model-based estimation of microscopic anisotropy using diffusion MRI: a simulation study. NMR in Biomedicine 2016;29(5):672–685.

[29] Westin CF, Knutsson H, Pasternak O, Szczepankiewicz F, Özarslan E, van Westen D, et al. Q-space trajectory imaging for multidimensional diffusion MRI of the human brain. Neuroimage 2016;135:345–362.

[30] Kaden E, Kruggel F, Alexander DC. Quantitative mapping of the per-axon diffusion coefficients in brain white matter. Magnetic resonance in medicine 2016;75(4):1752–1763.

[31] Callaghan P, Jolley K, Lelievre J. Diffusion of water in the endosperm tissue of wheat grains as studied by pulsed field gradient nuclear magnetic resonance. Biophysical journal 1979;28(1):133–141.

[32] Edén M. Computer simulations in solid-state NMR. III. Powder averaging. Concepts in Magnetic Resonance Part A: An Educational Journal 2003;18(1):24–55.

[33] Lampinen B, Szczepankiewicz F, Mårtensson J, van Westen D, Sundgren PC, Nilsson M. Neurite density imaging versus imaging of microscopic anisotropy in diffusion MRI: a model comparison using spherical tensor encoding. Neuroimage 2017;147:517–531.

[34] Veraaart J, Fieremans E, Rudrapatna U, Jones DK, Novikov DS. Breaking the power law scaling of the dMRI signal on the Connectom scanner reveals its sensitivity to axon diameters. In: Proceedings of the 26th Annual Meeting of ISMRM, Paris, France; 2018. .

[35] Jones DK, Horsfield MA, Simmons A. Optimal strategies for measuring diffusion in anisotropic systems by magnetic resonance imaging. Magnetic Resonance in Medicine: An Official Journal of the International Society for Magnetic Resonance in Medicine 1999;42(3):515–525.

[36] Caruyer E, Lenglet C, Sapiro G, Deriche R. Design of multishell sampling schemes with uniform coverage in diffusion MRI. Magnetic resonance in medicine 2013;69(6):1534–1540.

[37] Jones DK, Alexander DC, Bowtell R, Cercignani M, Dell'Acqua F, McHugh DJ, et al. Microstructural imaging of the human brain with a 'super-scanner': 10 key advantages of ultra-strong gradients for diffusion MRI. NeuroImage 2018;182:8–38.

[38] Tax CM, Szczepankiewicz F, Nilsson M, Jones DK. The dot-compartment revealed? Diffusion MRI with ultra-strong gradients and spherical tensor encoding in the living human brain. bioRxiv 2019;p. 584730.

[39] Vangelderen P, DesPres D, Vanzijl P, Moonen C. Evaluation of restricted diffusion in cylinders. Phosphocreatine in rabbit leg muscle. Journal of Magnetic Resonance, Series B 1994;103(3):255–260.

[40] de Almeida Martins JP, Topgaard D. Two-dimensional correlation of isotropic and directional diffusion using NMR. Physical review letters 2016;116(8):087601.

[41] Aboitiz F, Scheibel AB, Fisher RS, Zaidel E. Fiber composition of the human corpus callosum. Brain research 1992;598(1-2):143–153.

[42] Caminiti R, Ghaziri H, Galuske R, Hof PR, Innocenti GM. Evolution amplified processing with temporally dispersed slow neuronal connectivity in primates. Proceedings of the National Academy of Sciences 2009;p. pnas–0907655106.

[43] Aja-Fernández S, Vegas-Sánchez-Ferrero G. Statistical analysis of noise in MRI. Switzerland: Springer International Publishing 2016;.

[44] Jones DK, Basser PJ. Squashing peanuts and smashing pumpkins": how noise distorts diffusion-weighted MR data. Magnetic Resonance in Medicine: An Official Journal of the International Society for Magnetic Resonance in Medicine 2004;52(5):979–993.

[45] Kellner E, Dhital B, Kiselev VG, Reisert M. Gibbs-ringing artifact removal based on local subvoxel-shifts. Magnetic resonance in medicine 2016;76(5):1574–1581.

[46] Andersson JL, Sotiropoulos SN. An integrated approach to correction for off-resonance effects and subject movement in diffusion MR imaging. Neuroimage 2016;125:1063–1078.

[47] Dhital B, Reisert M, Kellner E, Kiselev VG. Intra-axonal diffusivity in brain white matter. NeuroImage 2019;189:543–550.

[48] Zhang Y, Brady M, Smith S. Segmentation of brain MR images through a hidden Markov random field model and the expectation-maximization algorithm. IEEE transactions on medical imaging 2001;20(1):45–57.

[49] Jensen JH, Helpern JA. MRI quantification of non-Gaussian water diffusion by kurtosis analysis. NMR in Biomedicine 2010;23(7):698–710.

[50] Röding M, Bernin D, Jonasson J, Särkkä A, Topgaard D, Rudemo M, et al. The gamma distribution model for pulsed-field gradient NMR studies of molecular-weight distributions of polymers. Journal of Magnetic Resonance 2012;222:105–111.

[51] Szczepankiewicz F, Lasič S, van Westen D, Sundgren PC, Englund E, Westin CF, et al. Quantification of microscopic diffusion anisotropy disentangles effects of orientation dispersion from microstructure: applications in healthy volunteers and in brain tumors. NeuroImage 2015;104:241–252.

[52] Jensen JH, Helpern JA. Characterizing intra-axonal water diffusion with direction-averaged triple diffusion encoding MRI. NMR in Biomedicine 2018;31(7):e3930.